Journal of
Materials Chemistry A

COMMUNICATION

Cite this: *J. Mater. Chem. A*, 2019, 7, 17782

Received 14th May 2019
Accepted 15th July 2019

DOI: 10.1039/c9ta05063a

rsc.li/materials-a

In situ formation of a multicomponent inorganic-rich SEI layer provides a fast charging and high specific energy Li-metal battery†

Ho-Hyun Sun,[a] Andrei Dolocan,[b] Jason A. Weeks,[c] Rodrigo Rodriguez,[a] Adam Heller[a] and C. Buddie Mullins *[ac]

The performance of the rechargeable Li metal battery anode is limited by the poor ionic conductivity and poor mechanical properties of its solid-electrolyte interphase (SEI) layer. To overcome this, a 3 : 1 v/v ethyl methyl carbonate (EMC) : fluoroethylene carbonate (FEC) containing 0.8 M lithium bis(trifluoromethanesulfonyl)imide (LiTFSI) and 0.2 M lithium difluoro(oxalate)borate (LiDFOB) dual-salts with 0.05 M lithium hexafluorophosphate ($LiPF_6$) was tested to promote the formation of a multitude of SEI-beneficial species. The resulting SEI layer was rich in LiF, Li_2CO_3, oligomeric and glass borates, Li_3N, and Li_2S, which enhanced its role as a protective yet Li^+ conductive film, stabilizing the lithium metal anode and minimizing dead lithium build-up. With a stable SEI, a Li/Li[$Ni_{0.59}Co_{0.2}Mn_{0.2}Al_{0.01}$]$O_2$ Li-metal battery (LMB) retains 75% of its 177 mA h g^{-1} specific discharge capacity for 500 hours at a coulombic efficiency of greater than 99.3% at the fast charge–discharge rate of 1.8 mA cm^{-2}.

Introduction

After years of successful use of the 372 mA h g^{-1} specific capacity lithium-ion battery (LIB) graphite anode, the demand for higher energy-density batteries and the LIB capacity limitation imposed by intercalation chemistry[1–4] intensified the long-simmering interest in the 3860 mA h g^{-1} specific capacity metallic lithium anode. Were it not for its Li^+-flux retarding SEI, the metallic Li could offer fast rate in a highly ionically conductive electrolyte and its low redox potential (−3.004 *vs.* standard hydrogen electrode) could increase the energy of cells.[5,6] Despite its promise, metallic Li does not cycle stably as the dendritic growth and the parasitic reaction of Li with the electrolyte causes loss of both electrolyte and of active lithium.[7–9]

To overcome these issues, the focus has shifted toward using a combination of electrolyte, salt, and additives to *in situ* establish a stable solid-electrolyte interphase (SEI) layer as a protective and ionically conductive film on the lithium metal surface.[10–12] The SEI is vital to the stable cycling of Li metal and its efficacy depends heavily on its composition. In this regard, numerous electrolyte solutions and resulting SEI layers have been reported. In particular, fluorinated electrolyte combinations have been studied to increase the LiF content in the SEI to enhance its protective capability since LiF-rich SEI passivates the lithium metal/electrolyte interface; it is electrochemically stable and has low electrical conductivity.[13–16] Other SEIs, heavy in Li_2CO_3, Li_2O, Li_2S, and Li_3N species, have also been reported to effectively enhance the mechanical stability and ionic conductivity of the SEI.[17–21] However, studies focusing on combinations of multiple SEI-beneficial compounds have been lacking.

Here, we report a SEI layer capable of maintaining the reversibility of lithium for long-term cycling by promoting the formation of SEI-beneficial species. In this endeavor, we employ a fluoroethylene carbonate (FEC)-based electrolyte to form a LiF-rich SEI layer coupled with lithium bis(trifluoromethanesulfonyl)imide (LiTFSI) and lithium difluoro(oxalate)borate (LiDFOB) dual-salts to introduce Li_3N/Li_2S and Li_2CO_3/O–B–O oligomeric and glass borates, respectively, to further reinforce the ionic conductivity and mechanical integrity of the SEI layer. As the extensive X-ray photoelectron spectroscopy (XPS) and time-of-flight secondary-ion mass spectrometry (TOF-SIMS) analysis delineate, the as-formed SEI layer was rich not only in LiF, but also in Li_3N, Li_2S, Li_2CO_3, and O–B–O oligomeric borates. The resulting SEI layer proved to be efficacious in stabilizing the lithium electrode by reducing the amount of electrically disconnected lithium. Reflecting its diversity in SEI-beneficial compounds, the 0.8 M LiTFSI + 0.2 M LiDFOB + 0.05 M $LiPF_6$ in EMC : FEC = 3 : 1 v/v LMB cell delivered a performance of 75% capacity retention after 500

---

[a] *McKetta Department of Chemical Engineering, The University of Texas at Austin, Texas 78712-1589, USA. E-mail: mullins@che.utexas.edu*

[b] *Texas Materials Institute, University of Texas at Austin, Austin, Texas 78712-1224, USA*

[c] *Department of Chemistry, The University of Texas at Austin, Texas 78712-1224, USA*

† Electronic supplementary information (ESI) available. See DOI: 10.1039/c9ta05063a

cycles (Li *vs.* Li[$Ni_{0.59}Co_{0.2}Mn_{0.2}Al_{0.01}$]$O_2$ cathode) with coulombic efficiencies exceeding 99.3% at a current density of 1.8 mA cm^{-2} and discharge capacity of 1.77 mA h g^{-1}.

Results and discussion

SEI layer surface XPS characterization

An ideal SEI is one that is permeable to Li^+, is ductile yet strong enough to withstand the mechanical stress associated with its compositional and dimensional changes upon cycling, and is insoluble in the electrolytic solution throughout its cycling-potential range. These qualities of the SEI depend heavily on its chemical composition and will facilitate the stable cycling of the lithium metal anode. We employed a FEC-based electrolyte in order to form a LiF-rich SEI layer. LiTFSI was the main salt of choice as it introduces species that contribute to the important SEI features discussed above and LiDFOB was added to further strengthen the SEI layer. The $LiPF_6$ salt was mixed in as an additive to prevent Al corrosion.[22]

Three electrolyte solutions: (i) 1 M of LiTFSI + 0.05 M of $LiPF_6$ in EMC : FEC = 3 : 1 (referred to as 10EF31P), (ii) 0.6 M of LiTFSI + 0.4 M of LiDFOB + 0.05 M of $LiPF_6$ in EMC : FEC = 3 : 1 (referred to as 64EF31P), and (iii) 0.8 M of LiTFSI + 0.2 M of LiDFOB + 0.05 M of $LiPF_6$ in EMC : FEC = 3 : 1 (referred to as 82EF31P) were synthesized and X-ray photoelectron spectroscopy (XPS) was performed on the SEI after the first deposition in Li/Cu cells to ascertain their chemical composition. The F1s, O1s, B1s, and N1s spectra are shown in Fig. 1 and S2p and C1s are shown in Fig. S1.† As expected of the electrochemical decomposition from the FEC solvent and fluorine containing anions $TFSI^-$, $DFOB^-$, and PF_6^-, the peak corresponding to Li–F (684.5 eV) was observed in the F1s spectra for all three electrolytes (Fig. 1a–c) with the 82EF31P SEI exhibiting an especially strong Li–F peak, followed by that of the 64EF31P SEI. Similarly, the Li_2CO_3 peak (531.8 eV) appeared stronger for the 82EF31P SEI compared to the other two SEIs in the O1s spectra (Fig. 1d–f); LiF is produced in reactions of metallic Li with FEC and the fluorine containing anions $TFSI^-$, $DFOB^-$, and PF_6^- and Li_2CO_3

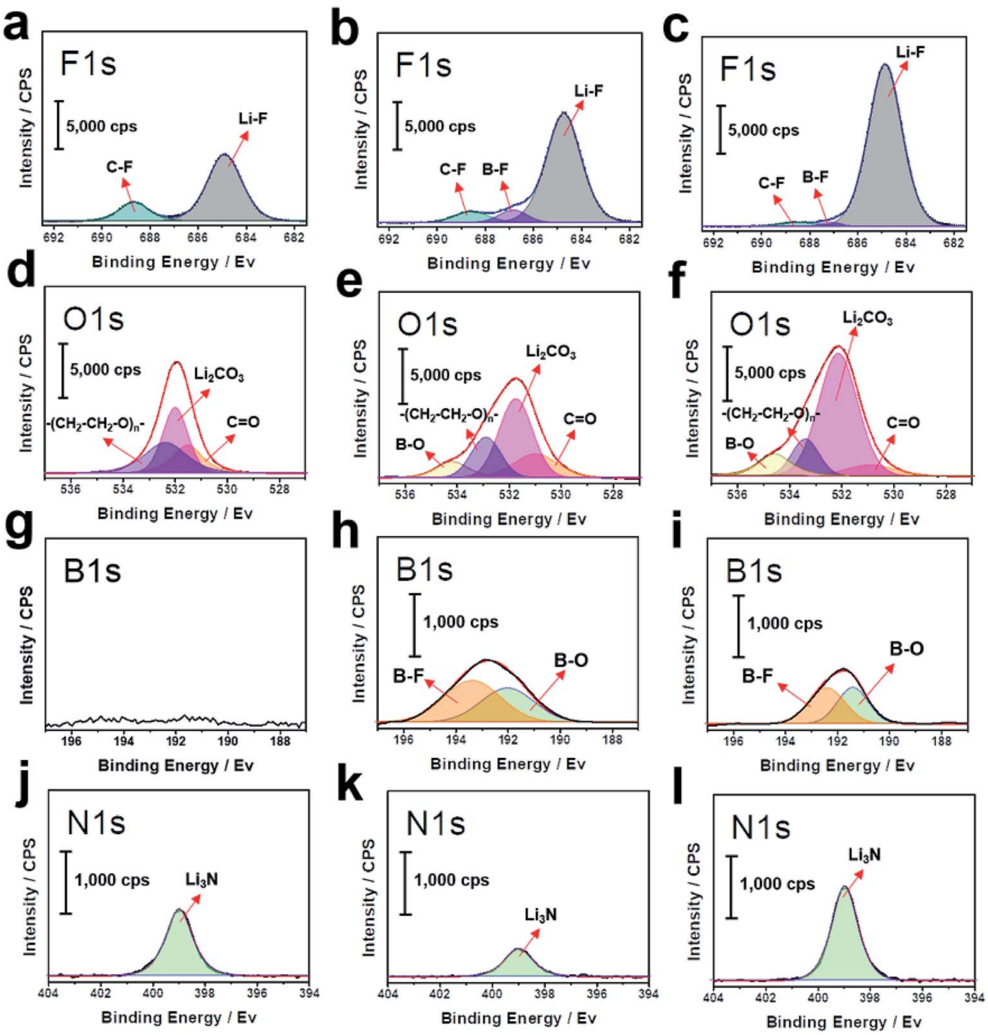

Fig. 1 XPS spectra of F1s (a–c), O1s (d–f), B1s (g–i) and N1s (j–l) of the SEI layer surface after 1st deposition in Li/Cu cells: (a, d, g and j) 10EF31P, (b, e, h and k) 64EF31P, and (c, f, i and l) 82EF31P.

is produced when metallic Li reacts with the carbonate solvents. These two peaks are of interest because LiF and Li_2CO_3 are less soluble in solvents and have a high Young's modulus of 64.9 Gpa and 75.0 Gpa,[23] contributing greatly to the physicochemical stability of the Li metal SEI. Yet despite their advantageous property, LiF and Li_2CO_3 are ionic insulators with conductivities of $\sim 10^{-12}$ S cm^{-1} and $\sim 10^{-15}$ S cm^{-1},[24,25] respectively, and limit the transport of Li^+ during fast charging. Fortunately, the integration of crystalline oligomeric borates like $Li_2B_4O_7$ and lithium borate glasses and Li_3N balances the drawback in ionic conductivity. The former are fast Li^+ conductors with conductivities greater than 10^{-7} S cm^{-1} which derive from the borate oligomer comprising oxygen double-bonded to boron to which Li^+ from proximal anionic oxygens single-bonded to boron can hop[26–29] and the latter has a high conductivity of 10^{-4} S cm^{-1}.[30] Since borates originate from LiDFOB, the borate B–O peak can be seen at 191.7 eV in the B1s spectra and at 534.6 eV in the O1s spectra (Fig. 1d–i). The peak corresponding to the Li_3N can be seen at 399.1 eV in the N1s spectra (Fig. 1j–l) and appeared the strongest in the 82EF31P SEI and weakest in the 64EF31P SEI.

Another component to consider is the quantity of organic compounds in the SEI layer. Organic matters are less desirable because they are not as physiochemically stable as inorganic compounds[31,32] and are prone to SEI damage due to having a low Young's modulus (less than 1 Gpa),[23] leading to dead lithium accumulation during prolonged cycling to hinder Li transport and accelerate dendrite nucleation and growth. Conversely, inorganic components are less soluble in electrolyte[33] and their high Young's modulus[23] increases the SEI mechanical strength and their Li^+ conductive nature makes inorganic-rich SEI more suitable during fast charge conditions where the SEI layer is under severe stress. In XPS, organic compounds are represented by the $-(CH_2-CH_2-O)_n-$ and C=O peaks at 533.5 and 530.5 eV in the O1s spectra (Fig. 1d–f). Interestingly, the intensities of these peaks were opposite to inorganic compound intensities where the inorganic-rich 82EF31P SEI exhibited the weakest $-(CH_2-CH_2-O)_n-$ and C=O signals while inorganic-poor 10EF31P SEI showed the strongest organic signals which is in agreement with a recent report.[34] The inverse relationship suggests that when insoluble and nonporous films of inorganic lithium salts are formed, as is the case in 82EF31P, excessive solvent reduction is prevented.

Deposition morphology and Li/Li electrochemical cycling

The composition of the SEI layer profoundly affected the deposition morphology of lithium as seen in the scanning electron microscope (SEM) images of lithium deposited on Cu foil in 2032-coin cells cycled at a fast charge rate of 1.8 mA cm^{-2} for 1 hour (Fig. 2a–f).[24,35] As the SEM images present, the 10EF31P deposited lithium appeared as a network of

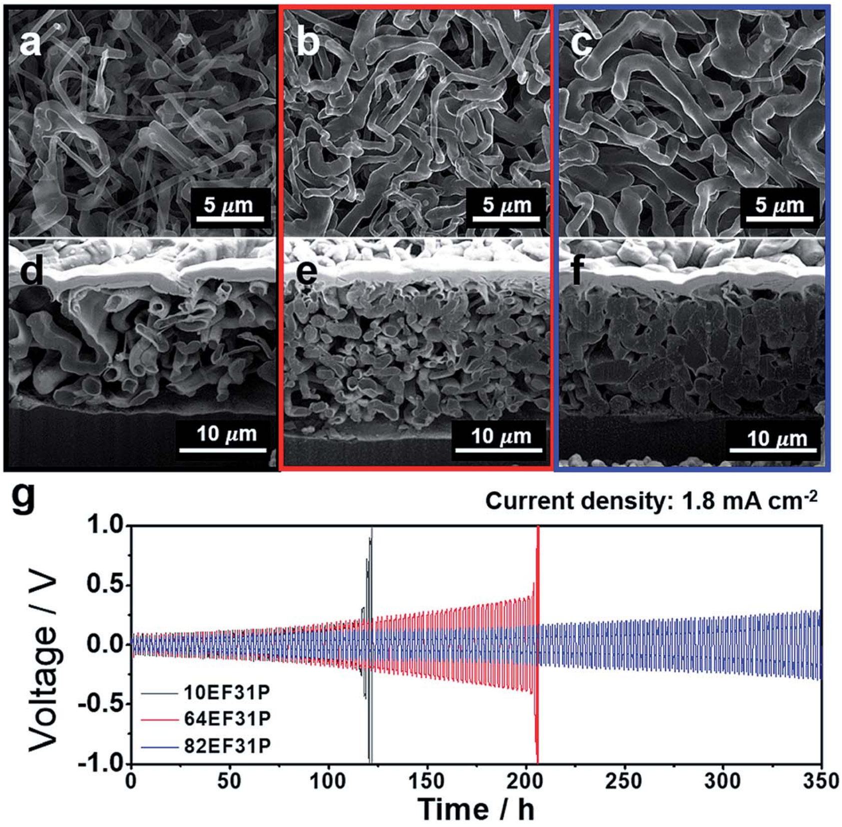

Fig. 2 Comparison of deposited Li morphologies (top view a–c) and their cross-sectional SEM images (d–f). The Li was deposited on Cu-foil: (a and d) in the 10EF31P electrolyte, (b and e) 64EF31P, and (c and f) 82EF31P. (g) Voltage excursions during the galvanostatic Li deposition/stripping cycles of Li/Li cells at 1.8 mA cm^{-2} with the three different electrolytes.

intertwined wires, but the lithium structures were uneven, loosely-packed, and consisted of thin wires of $\sim$0.6 μm diameter. The 64EF31P showed a better deposition morphology but its packing density was mediocre and was comprised of a mixture of thin and thick wires, likely due to a lack of ionic conductivity enhancing species.[36] In contrast, the 82EF31P SEI layer, which was rich in SEI-beneficial species, displayed a substantially improved deposition morphology with lithium being deposited densely as $\sim$1.2 μm thick microwire structures. At a lower current density of 0.9 mA cm^{-2} (Fig. S2†), a similar trend is observed, albeit more amplified. Moreover, the impact the SEI has on deposition morphology becomes more evident when lithium is deposited freely at 1.8 mA cm^{-2} for 1 hour in a Li/Li optical cell as observed in Fig. S3.† As the optical images reveal, when no pressure is applied, the 10EF31P and 64EF31P deposited lithium in a loose dendritic morphology whereas the 82EF31P deposited lithium in a uniform and compact morphology.

Such differences in Li deposition morphologies can be further explained by the dendrite nucleation time, which follows a Sand's time relationship:[37]

$$t_{\mathrm{Sand}} = \pi D_{\mathrm{app}} \frac{(z_{\mathrm{c}} c_0 F)^2}{4(J t_{\mathrm{a}})^2}$$

where t_{Sand} is the time required for dendrites to nucleate, D is the ambipolar diffusion constant, e is the electronic charge, c_0 is the initial concentration, J is the applied current density, and t_{a} is the anion transference number ($t_{\mathrm{a}} = 1 - t_{\mathrm{Li}^+}$). From the equation, it can be deduced that a higher Li$^+$ transference number (t_{Li^+}) results in a larger t_{Sand}, meaning that the SEI more effectively suppresses dendrite growth. Li$^+$ transference numbers were determined through electrochemical impedance spectroscopy (EIS) and chronoamperometry experiments (Fig. S4†) according to the Bruce and Vincent method[38] using Li/Li cells; the corresponding equivalent circuit of the EIS Li/Li cells is shown in Fig. S5.† The resulting transference numbers

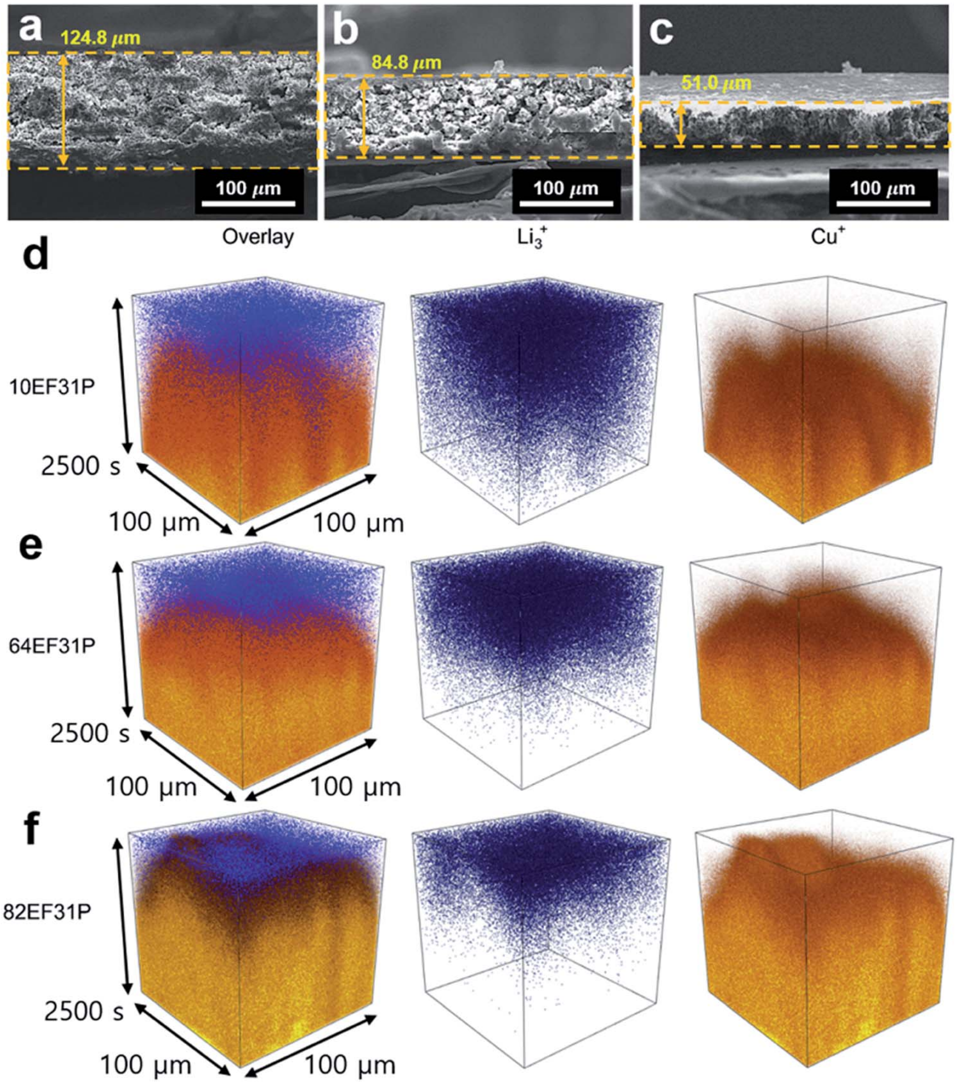

Fig. 3 Cross-section views of cycled dead lithium layer collected from Li/Cu cells of (a) 10EF31P, (b) 64EF31P, and (c) 82EF31P after 50 deposition/stripping cycles. TOF-SIMS 3D view of the dead lithium (represented by the Li_3^+ fragment) throughout the SEI in the (d) 10EF31P, (e) 64EF31P, and (f) 82EF31P samples We find the least amount of dead lithium in the 82EF31P SEI layer.

of the different SEIs were $t_{\mathrm{Li}^+} = 0.476$ for 10EF31P, $t_{\mathrm{Li}^+} = 0.493$ for 64EF31P and $t_{\mathrm{Li}^+} = 0.525$ for 82EF31P, respectively (Table S1†). Note that the initial current was calculated using Ohm's law: $I_0 = \Delta V(R_\mathrm{b} + R_\mathrm{int})$. Additionally, the initial overpotential values of 10EF31P, 64EF31P, and 82EF31P SEI layers (Fig. S6†), which were −0.0731 V, −0.05438 V, and −0.04842 V, respectively, show that the 82EF31P SEI experienced the least resistance in depositing Li through the SEI. Hence, the 82EF31P SEI layer effectively delays the dendrite nucleation time and facilitates lithium deposition to induce a dense and thick Li deposition morphology.

The electrochemical performance of symmetrical Li/Li cells of the different electrolytes cycled galvanostatically at 1.8 mA cm^{-2}, are illustrated in Fig. 2g. As augured by its poor deposition morphology and unfavorable chemical composition, the 10EF31P Li/Li cell showed progressively increasing overpotential curves and failed prematurely with a sudden voltage polarization at 120 hours, suggesting a heavy dead Li build-up. The 64EF31P cell cycled longer but also failed at 205 hours with an accelerated overpotential increase towards the end of its cycle life. On the other hand, the 82EF31P cell demonstrated a stable deposition/stripping cycling with minimal overpotentials for more than 350 hours which mirrors its favorable chemical composition and deposition structures. Similarly, under strenuous conditions of a very high current density of 3.6 mA cm^{-2}, the 82EF31P cell cycled to over 200 hours with suppressed overpotential while 10EF31P and 64EF31P cells failed at 74 and 82 hours, respectively (Fig. S7†). At a lower current density of 0.9 mA cm^{-2}, no distinguishable changes between the three different electrolyte cells were seen up to 500 hours (Fig. S8†). The ionic conductivities (Table S2†) of the 10EF31P, 64 EF31P, and 82EF31P were calculated to be 2.39 × 10^{-3}, 2.04 × 10^{-3}, and 2.26 × 10^{-3} S cm^{-1}, respectively, which matches the trend observed in a previous report[39] where the addition of LiDFOB to a LiTFSI-based solution lowers the ionic conductivity of the electrolyte; the large TFSI$^-$ anion size reduces interionic interaction and leads to a higher ionic mobility.[40,41] However, it should be noted that Li$^+$ transport in the cell is affected by other factors such as SEI surface resistance and charge transfer resistance, and the amalgamation of these components enables the improved cycling of the 82EF31P cell.

Dead Li layer

With each cycle, some of the lithium is lost as dead lithium that accumulates in the SEI layer. Fig. 3a–c reveal the extent of Li loss after 50 deposition/stripping cycles in the Li/Cu cells, reflecting the efficacy of the SEI layer in preventing dead Li formation. The dead Li thicknesses were 124.8 μm, 84.8 μm, and 51.0 μm for 10EF31P, 64EF31P, and 82EF31P. To better quantify the extent of dead Li in the SEI layer, time-of-flight secondary-ion mass spectrometry (TOF-SIMS) depth profiling in positive polarity with a O_2^+ sputtering beam (∼500 nA, 2 keV) was employed and the three-dimensional (3D) view of the Li_3^+ (representing the dead lithium) and Cu$^+$ (representing the bulk Cu foil) depth profiles for the 10EF31P, 64EF31P, and 82EF31P samples are presented in Fig. 3d–f. Given the nature of the TOF-SIMS technique, which is based on fragmentation of the surface compounds, larger clusters consisting of the same element (such as Li_3^+) are usually representative of that element's bulk material (in this case, dead/bulk Li). Clearly, the thicknesses of the dead lithium layer match those seen in the cross-sectional SEM images and the dead lithium accounts for a larger amount in the SEI of 10EF31P. While a similar amount of inactive Li was present on the surface for the three SEI layers (Fig. S9†), the area under the curve

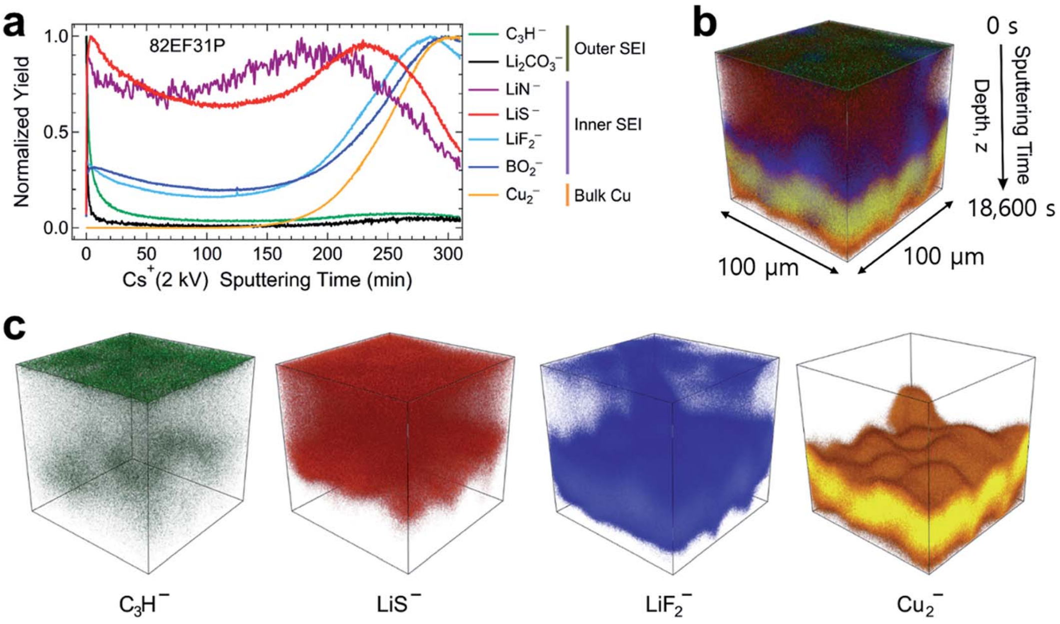

Fig. 4 (a) TOF-SIMS depth profiles (normalized to maximum) of various species of interest acquired from the 82EF31P sample (in Li/Cu cell) with a Cs$^+$ at 2 kV ion energy sputtering beam. The chemical composition and depth localization of different layers of the SEI are identified: C_3H^-, $Li_2CO_3^-$, LiS$^-$, LiF$_2^-$ and BO$_2^-$. (b and c) 3D view of the depth profiles in (a) showing the spatial localization of various species composing the SEI.

(proportional to the total amount of dead lithium) was much less for 82EF31P SEI at 2868 counts compared to the other two SEI layers with 4833 counts (10EF31P) and 4396 counts (64EF31P). It should also be noted that the Li_3^+ signals of 10EF31P and 64EF31P were likely reduced due to the uneven and porous dead Li structures of 10EF31P and 64EF31P SEI layer that were significantly changing the effective acquisition area. Moreover, the average coulombic efficiencies (CEs) of 10EF31P, 64EF31P, and 82EF31P were 97.0%, 98.3%, and 98.8%, respectively, which further lend credence that the maximization of SEI-beneficial compounds suppresses active Li loss (Fig. S10 and Table S3†); regular coulombic efficiencies are shown in Fig. S11.† Likewise, the electrochemical impedance spectroscopy (EIS) value for 82EF31P Li/Cu cells experienced the least increase in resistance after 50 cycles (Fig. S12 and Table S4†).

Full SEI layer TOF-SIMS chemical reconstruction

Indeed, the deposited lithium morphologies, deposition/stripping cycling performance, and dead Li quantity, all point to the 82EF31P solution providing a superior SEI layer relative to the 10EF31P and 64EF31P solutions. To gain more insight into the 82EF31P SEI layer, TOF-SIMS depth profiling was used to chemically reconstruct the full-depth of the 82EF31P SEI layer (as tested in Li/Cu cells) since the standard XPS depth of information is surface limited (less than 10 nm).[42,43] Fig. 4a shows the normalized to maximum depth profiles of various species of interest forming the SEI. Depth profile normalization is used to demonstrate the localization of various layers of the SEI : C_3H^- and $Li_2CO_3^-$ (corresponding to the organic part of the SEI and Li_2CO_3, respectively) reside mostly on the SEI surface; LiS^-, LiF_2^- and BO_2^- (corresponding to Li_2S, LiF, and oligomeric and glass borates, respectively) form the inner part of the SEI, while Cu_2^- corresponds to the bulk Cu foil electrode. The 3D views of these profiles are delineated in Fig. 4b and c, demonstrating the stratified structure of the SEI. Here, a Cs^+ ion beam (~70 nA, 2 keV) was used for sputtering in order to penetrate completely through the SEI and reach the Cu substrate. An important point to note here is that Li_2S, which

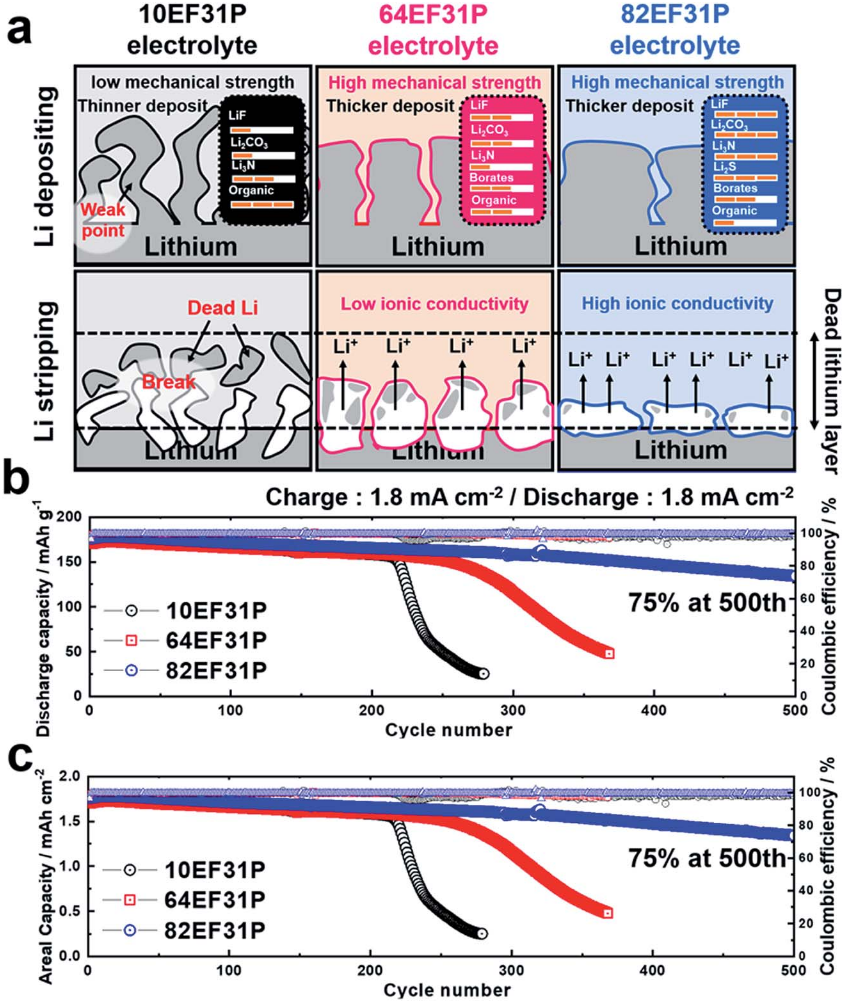

Fig. 5 (a) Proposed illustration summarizing the multicomponent inorganic-rich SEI layer of 82EF31P (blue) compared to the SEIs of 10EF31P (black) and 64EF31P (red). Long-term cycling performance of a Li/NCM622 cell with 10EF31P, 64EF31P, and 82EF31P electrolyte solutions as a function of (b) discharge capacity (mA h g^{-1}) and (c) coulombic efficiency with a cathode loading of 10 mg cm^{-2} cycled at a high current density of 1.8 mA cm^{-2}.

was absent in the XPS spectra, appeared remarkably strongly and evenly below the surface. Li_2S is of particular interest because it contributes concurrently to both mechanical robustness (Young's modulus of 82.6 Gpa)[23] and ionic conductivity ($\sim 10^{-5}$ S cm^{-1})[44] and is produced during the cycling.

82EF31P SEI layer mechanism and LMB electrochemical performance

How the chemical composition of the SEI layer influences its potency and subsequent deposition morphology/active lithium retention is illustrated in Fig. 5a. The 10EF31P SEI is mechanically weak due to the lack of LiF and Li_2CO_3 which results in the deposited lithium breaking off at weak points to leave behind electrically disconnected dead Li. In contrast, the 64EF31P SEI possesses high structural modulus but is low in ionic conductivity due to poor Li_3N content and experiences difficulty with Li^+ transport. Only the 82EF31P SEI layer features both high mechanical strength and ionic conductivity due to the minimization of organic compounds and ample integration of SEI-beneficial compounds in the SEI.

As a result, when coupled with a cathode in a proto-type lithium-metal anode battery, the 82EF31P dual-salt electrolyte cell displayed a promising electrochemical performance as seen in Fig. 5b and c where the former is in discharge capacity (mA h g^{-1}) and the latter is coulombic efficiency. At a rapid charge–discharge rate of 1.8 mA cm^{-2} and a high $Li[Ni_{0.59}Co_{0.2}Mn_{0.2}Al_{0.1}]O_2$ (NCM622-Al 1%) cathode loading of 10 mg cm^{-2}, the 82EF31P cell delivered a specific discharge capacity of 177 mA h g^{-1} and stable cycling with 75% capacity retention after 500 cycles. In contrast, the 10EF31P and 64EF31P cells failed prematurely similarly to the Li/Li symmetrical cell performance. The voltage profiles of the 10EF31P, 64EF31P, and 82EF31P Li/NCM cells are presented in Fig. S13.† Note that the $Li[Ni_{0.6}Co_{0.2}Mn_{0.2}]O_2$ cathode was doped with 1% Al to increase the structural integrity of the cathode particle, minimizing capacity loss due to cathode concerns.[45,46] Moreover, despite having large amounts of Li being passed back and forth in cycling, the 82EF31P electrolyte was able to maintain coulombic efficiencies higher than 99.3% throughout its 500 cycles, implying comparatively little loss of active lithium. As a control, we have also tested the Li/Li and Li/NCM cycling performances of 1.05 M LiTFSI and 1.05 M $LiPF_6$ in EMC : FEC = 3 : 1 electrolytes as shown in Fig. S14 and 15.† The promising performance of the 82EF31P electrolyte-SEI cell is also reflected in its rate capability performance at various C-rates (Fig. S16†) where the 82EF31P cell outperformed the 10EF31P and 64EF31P cells. The performance demonstrated by 82EF31P at higher C-rates can be ascribed to the inorganic compounds being well-distributed throughout the SEI, enabling the transport of lithium through the SEI. Table S5† compares the electrochemical performance of the 82EF31P dual-salt electrolyte to other electrolyte solutions. The promising performance shown by the 82EF31P cell is possible because the holistic inclusion of LiF, Li_2CO_3, Li_3N, Li_2S, and oligomeric and glass borates in the SEI layer bolsters its role as a protection layer and ionic conductor, thereby enabling the SEI layer to stabilize the lithium-metal anode for use in a long-term high energy density LMB.

Conclusion

In summary, a multicomponent inorganic-rich SEI layer was designed through the combination of LiTFSI and LiDFOB salts dissolved in a FEC-based electrolyte. The 0.8 M LiTFSI + 0.2 M LiDFOB + 0.05 M $LiPF_6$ in EMC : FEC = 3 : 1 (82EF31P) electrolyte solution introduced a multitude of SEI-beneficial inorganic compounds (LiF, Li_2CO_3, Li_3N, Li_2S, and cross-linked O–B–O oligomeric and glass borates) into the SEI layer while the preferential reduction of salts over carbonate electrolytes significantly lowered the content of organic compounds in the SEI layer. The resulting inorganic-rich composition substantially enhanced the mechanical robustness and ionic conductivity of the SEI layer, enabling the stabilization and preservation of the active lithium-metal. Consequently, the resulting SEI layer enabled the Li/Li cell to deliver a stable deposition/stripping cycling for more 350 hours and the Li/Li$[Ni_{0.59}Co_{0.2}Mn_{0.2}Al_{0.01}]O_2$ lithium-metal battery to deliver an overall 75% capacity retention at 500 cycles with greater than 99.3% coulombic efficiencies at a current density and specific discharge capacity of 1.8 mA cm^{-2} and 177 mA h g^{-1}, respectively. Through this work, we hope to demonstrate that a multi-inorganic SEI layer is more efficacious in its role as a protective and ionically conductive layer than SEI layers concentrated with a single beneficial species. Future efforts to further increase the content of the aforementioned species or add other inorganic compounds through additives could better stabilize and preserve lithium metal for a superior performance lithium-metal battery.

Conflicts of interest

The authors declare no competing financial interest.

Abbreviations

EMC	Ethyl methyl carbonate
FEC	Fluoroethylene carbonate
LiTFSI	Lithium bis(trifluoromethanesulfonyl)imide (LiTFSI)
LiDFOB	Lithium difluoro(oxalate)borate
$LiPF_6$	Lithium hexafluorophosphate
10EF31P	1 M LiTFSI + 0.05 M $LiPF_6$ in EMC : FEC = 3 : 1 v/v
64EF31P	0.6 M LiTFSI + 0.4 M LiDFOB + 0.05 M $LiPF_6$ in EMC : FEC = 3 : 1 v/v
82EF31P	0.8 M LiTFSI + 0.2 M LiDFOB + 0.05 M $LiPF_6$ in EMC : FEC = 3 : 1 v/v
NCM622-Al 1%	Layered $Li[Ni_{0.59}Co_{0.2}Mn_{0.2}Al_{0.1}]O_2$ cathode
SEI	Solid-electrolyte interphase
EIS	Electrochemical impedance spectroscopy
SEM	Scanning electron microscope
XPS	X-ray photoelectron spectroscopy
TOF-SIMS	Time-of-flight secondary-ion mass spectrometry

Acknowledgements

The authors gratefully acknowledge support from the Welch Foundation *via* Grants F-1131 (AH) and F-1436 (CBM) and also the National Science Foundation through Grant No. CBET-1603491. The authors also thank Professor Yang-Kook Sun of Hanyang University for providing the Li[$Ni_{0.6}Co_{0.2}Mn_{0.2}$]O_2 hydroxide precursors and Dr Hugo Celio for assisting with XPS measurements.

References

1 M. Armand and J. M. Tarascon, *Nature*, 2008, **451**, 652–657.
2 M. Winter, B. Barnett and K. Xu, *Chem. Rev.*, 2018, **118**, 11433–11456.
3 M. R. Palacin, *Chem. Soc. Rev.*, 2009, **38**, 2565–2575.
4 D. Lin, Y. Liu and Y. Cui, *Nanotechnology*, 2017, **12**, 194–206.
5 J. B. Goodenough and Y. Kim, *Chem. Mater.*, 2010, **22**, 587–603.
6 P. G. Bruce, S. A. Freunberger, L. J. Hardwick and J. M. Tarascon, *Nat. Mater.*, 2012, **11**, 19–29.
7 L. Ji, Z. Lin, M. Alcoutlabi and X. Zhang, *Energy Environ. Sci.*, 2011, **4**, 2682–2699.
8 S.-O. Tung, S. Ho, M. Yang, R. Zhang and N. A. Kotov, *Nat. Commun.*, 2015, **6**, 6152.
9 C.-P. Yang, Y.-X. Yin, S.-F. Zhang, N.-W. Li and Y.-G. Guo, *Nat. Commun.*, 2015, **6**, 8058.
10 W. Xu, J. Wang, F. Ding, X. Chen, E. Nasybulin, Y. Zhang and J.-G. Zhang, *Energy Environ. Sci.*, 2014, **7**, 513–537.
11 X.-B. Cheng and Q. Zhang, *J. Mater. Chem. A*, 2015, **3**, 7207–7209.
12 X.-B. Cheng, R. Zhang, C.-Z. Zhao, F. Wei, J.-G. Zhang and Q. Zhang, *Adv. Sci.*, 2016, **3**, 1500213.
13 X.-Q. Zhang, X.-B. Cheng, X. Chen, C. Yan and Q. Zhang, *Adv. Funct. Mater.*, 2017, **27**, 1605989.
14 X. Fan, L. Chen, X. Ji, T. Deng, S. Hou, J. Chen, J. Zheng, F. Wang, J. Jiang, K. Xu and C. Wang, *Chem*, 2018, **4**, 174–185.
15 S. Jiao, X. Ren, R. Cao, M. H. Engelhard, Y. Liu, D. Hu, D. Mei, J. Zheng, W. Zhao, Q. Li, N. Liu, B. D. Adams, M. Cheng, J. Liu, J.-G. Zhang and W. Xu, *Nat. Energy*, 2018, **3**, 739–746.
16 S.-J. Park, J.-Y. Hwang, C. S. Yoon, H.-G. Jung and Y.-K. Sun, *ACS Appl. Mater. Interfaces*, 2018, **10**, 17985–17993.
17 L. Yu, S. Chen, H. Lee, L. Zhang, M. H. Engelhard, Q. Li, S. Jiao, J. Liu, W. Xu and J.-G. Zhang, *ACS Energy Lett.*, 2018, **3**, 2059–2067.
18 L. Suo, W. Xue, M. Gobet, S. G. Greenbaum, C. Wang, Y. Chen, W. Yang, Y. Li and J. Li, *Proc. Natl. Acad. Sci. U.S.A.*, 2018, **6**, 1156–1161.
19 K. Park and J. B. Goodenough, *Adv. Energy Mater.*, 2017, **7**, 1700732.
20 Y. Liu, D. Lin, P. Y. Yuen, K. Liu, J. Xie, R. H. Dauskardt and Y. Cui, *Adv. Mater.*, 2017, **29**, 1605531.
21 G. Li, Y. Gao, X. He, Q. Huang, S. Chen, S. H. Kim and D. Wang, *Nat. Commun.*, 2017, **8**, 850.
22 J. Zheng, M. H. Engelhard, K. Mei, S. Jiao, B. J. Polzin, J.-G. Zhang and W. Xu, *Nat. Energy*, 2017, **2**, 17012.
23 G. Wan, F. Guo, H. Li, Y. Cao, X. Ai, J. Qian, Y. Li and H. Yang, *ACS Appl. Mater. Interfaces*, 2018, **10**, 593–601.
24 X. Wang, M. Zhang, J. Alvarado, S. Wang, M. Sina, B. Lu, J. Bouwer, W. Xu, J. Xiao, J.-G. Zhang, J. Liu and Y. S. Meng, *Nano Lett.*, 2017, **17**, 7606.
25 S. Shi, Y. Qi, H. Li and L. G. Hector Jr, *J. Phys. Chem. C*, 2013, **117**, 8579–8593.
26 L. Xing, J. Zheng, M. H. Engelhard, D. Mei, Q. Li, S. Jiao, N. Liu, W. Zhao, J.-G. Zhang and W. Xu, *ACS Appl. Mater. Interfaces*, 2018, **10**, 2469–2479.
27 L. Xia, S. Lee, Y. Jiang, Y. Xia, G. Chen and Z. Liu, *ACS Omega*, 2017, **2**, 8741–8750.
28 M. Balkanski, R. F. Wallis, J. Deppe and M. Massot, *Mater. Sci. Eng., B*, 1992, **12**, 281–298.
29 T. Schedlbauer, S. Kruger, R. Schmitz, R. W. Schmitz, C. Schreiner, H. J. Gores, S. Passerini and M. Winter, *Electrochim. Acta*, 2013, **92**, 102–107.
30 W. Li, G. Wu, C. M. Araujo, R. H. Scheicher, A. Blomqvist, R. Ahuja, Z. Xiong, Y. Feng and P. Chen, *Energy Environ. Sci.*, 2010, **3**, 1524–1530.
31 R. L. Sacci, J. M. Black, N. Balke, N. J. Dudney, K. L. More and R. R. Unocic, *Nano Lett.*, 2015, **15**, 2011–2018.
32 E. Peled and S. Menkin, *J. Electrochem. Soc.*, 2017, **164**, A1703–A1719.
33 E. Peled and D. Golodnitsky, *Lithium-Ion Batteries: Solid-Electrolyte Interphase*, Imperial College, London, 2004, p. 1.
34 J.-Y. Hwang, S.-J. Park, C. S. Yoon and Y.-K. Sun, *Energy Environ. Sci.*, 2019, **12**, 2174–2184.
35 J. Steiger, G. Richter, M. Wenk, K. Dominik and R. Monig, *Electrochem. Commun.*, 2015, **50**, 11–14.
36 R. Miao, J. Yang, Z. Xu, J. Wang, Y. Nuli and L. Sun, *Sci. Rep.*, 2016, **6**, 21771.
37 P. Bai, J. Li, F. R. Brushett and M. Bazant, *Energy Environ. Sci.*, 2016, **9**, 3221–3229.
38 G. B. Appetecchi, G. Dautzenberg and B. Scrosati, *J. Electrochem. Soc.*, 1996, **143**, 6–12.
39 F. Li, Y. Gong, G. Jia, Q. Wang, Z. Peng, W. Fan and B. Bai, *J. Power Sources*, 2015, **295**, 47–54.
40 J. Leys, R. N. Rajesh, P. C. Menon, C. Glorieux, S. Longuemart, P. Nockemann, M. Pellens and K. Binnemans, *J. Chem. Phys.*, 2010, **133**, 034503.
41 V. Aravindan, J. Gnanaraj, S. Madhavi and H.-K. Liu, *Chem.–Eur. J.*, 2011, **17**, 14326–14346.
42 H. Chou, A. Ismach, R. Gosh, R. S. Ruoff and A. Dolocan, *Nat. Commun.*, 2015, **6**, 7482.
43 M. P. Griffin, R. Gearba, K. J. Stevenson, D. A. Vanden Bout and A. Dolocan, *J. Phys. Chem. Lett.*, 2017, **8**, 2764–2773.
44 R. A. Huggins, *Electrochim. Acta*, 1977, **22**, 773–781.
45 S. H. Park, K. S. Park and Y.-K. Sun, *Electrochim. Acta*, 2001, **31**, 1215–1222.
46 U.-H. Kim, S.-T. Myung, C. S. Yoon and Y.-K. Sun, *ACS Energy Lett.*, 2017, **2**, 1848–1854.